

Micromechanical testing of carbon fibers deposited by low-pressure laser-assisted chemical vapor deposition

R. Longtin^{a,b,*}, C. Fauteux^{a,b}, J. Pegna^a, M. Boman^b

^a Freeform Fabrication Laboratories, Department of Mechanical Engineering, École Polytechnique de Montréal, Box 6079, Station A, Montréal, Canada, PQ, H3C 3A7

^b Department of Materials Chemistry, The Ångström Laboratory, Uppsala University, Box 538, 751 21 Uppsala, Sweden

Received 13 September 2003; accepted 29 June 2004

Abstract

Carbon fibers were deposited directly from ethylene by laser-assisted chemical vapor deposition. The precursor gas pressures and the incident laser powers were varied. Micro-mechanical testing was carried out using a high-precision micro-manipulator. During three-point bend testing the fibers showed an elastic response, with no residual strain upon unloading, until fracture. The fibers' strength and Young's modulus are reported. A model for fiber fracture is proposed based on fiber cross-section analysis. Scanning electron microscopy was used to study the fiber cross-sections and the fiber surface morphology. The mechanical properties are related to the characteristic fiber microstructure investigated by Raman spectroscopy.

© 2004 Elsevier Ltd. All rights reserved.

Keywords: A. Carbon fibers; B. Laser irradiation, Chemical vapor deposition; C. Raman spectroscopy; D. Mechanical properties

1. Introduction

The search for new high-performance materials is of great importance in the materials processing industry. Inorganic and organic fibers have been used in a variety of applications ranging from textile related applications to the creation of super-resistant composite materials. Of the many different fibers, carbon fibers are especially interesting for their high strength-to-weight ratio. When corrected for density, their mechanical properties make them the strongest or stiffest materials available [1]. These fibers have high strength and modulus and are resistant to creep or fatigue. Perfectly graphitic fibers theoretically have the highest Young's modulus of about 1000 GPa due to the high degree of alignment of the graphene planes along the fiber axis [2].

Freeform fabrication by laser-assisted chemical vapor deposition (LCVD) allows the creation of three-dimensional micro-sized structures directly from the vapor phase from a variety of precursor gases [3]. More specifically, pure carbon fibers can be deposited directly by LCVD [3–6].

Based on diameter, fibers can be classified into 4 major groups as rods (diameters greater than 200 μm), as very large diameter fibers (diameters ranging from 100 to 200 μm), as micro-fibers (diameters between 1 and 25 μm) and as nanofibers (diameters ranging from 1 to 25 nm) [7]. The majority of high-aspect ratio structures produced by LCVD have diameters in the hundreds of microns and are generally referred to as fibers.

Unlike conventional fiber production techniques that require many different intermediate production steps such as polymer spinning, stretching and heating, LCVD provides the freedom to produce carbon fibers directly from the vapor phase from a variety of stable and cheap precursors. Simple changes in the process

* Corresponding author. Tel.: +1 514 3404711; fax: +1 514 3403246.
E-mail address: remi.longtin@polymtl.ca (R. Longtin).

parameters allow the production of fibers having different sizes, lengths and microstructures. Additionally, an LCVD setup can be modified to include process control systems [8,9].

An investigation of LCVD fibers has shown that they are graphitic in nature, with a radial change in microstructure [10]. A radial change in local mechanical properties was also observed [11]. An investigation of the mechanical properties of high pressure LCVD carbon fibers has already been published [12,13]. However, no information has been gathered on the bulk mechanical properties of low-pressure LCVD (LP-LCVD) fibers and on possible mechanical properties deposition parameters dependencies. Hence, to complete the investigation of laser-grown carbon fibers, a three-point bend test was devised and carried out with the use of a micro-manipulator. Specifically designed for mechanical testing of micro-machined beams [14], the manipulator has been successfully used to investigate the strength and elastic properties of silicon and boron micro-fibers also deposited by LCVD [15,16].

2. Experimental

2.1. Fiber deposition

Laser chemical vapor deposition is a processing technique that uses a focused laser beam to initiate and maintain a chemically driven deposition process. The laser beam locally heats a substrate exposed to a precursor gas. The gas decomposes by pyrolysis on the heated spot to leave a solid residue. By moving the laser beam or the substrate, a variety of three-dimensional structures can be produced via this process. This process can use most of the precursors employed in conventional chemical vapor deposition (CVD).

In this analysis, carbon fibers were deposited on a glassy carbon substrate directly from ethylene at different precursor gas pressures and incident laser powers using an LCVD system. A system schematic can be found in a related paper [11]. A Coherent model Innova 90 continuous wave argon ion laser with a Gaussian intensity profile, operated at 514.5 nm with a spot size of 88 μm , was used as light source. Tracking of the focus with a three-axis micro-positioning system allowed steady-state growth of uniform fibers.

2.2. Deposition parameters

A number of fibers were deposited at pressures of 275 up to 1000 mbar. The laser powers used, between 0.3 and 2 W, produced fibers of 35–240 μm in diameter. The average fiber length was 3 mm. Generally, the fibers produced were uniform with a constant diameter over

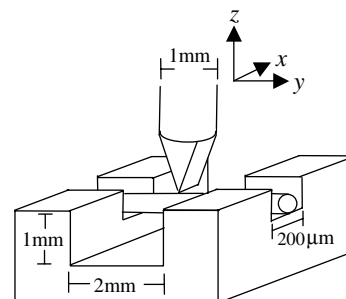


Fig. 1. Sample holder and wedge stylus (not to scale).

their entire length and had varying surface roughness from fiber to fiber.

2.3. Micro-mechanical testing

A wedge-shaped stylus attached to a micro-lever was used to apply a load at the center of the fibers. The manipulator had a force resolution of 0.1 mN. Various micro-manipulator specifications and a more detailed description can be found in a paper by Greek [14].

The fibers were placed across a 2 mm trench in 200 μm wide slits in a specifically designed brass sample holder seen in Fig. 1. The depth of the trench was 1 mm.

A CCD camera mounted in a stereomicroscope allowed real time observation and recording of the bending process with a maximum magnification of 100 \times . In this way deflection pictures at specific force values were taken. A LabView computer program was used for control and data acquisition. Before testing, the fiber diameters were measured with an accuracy of 0.3 μm using a microscope at 50 \times magnification. After fracture, the cross-sections were examined with an HR-SEM.

3. Results and discussion

3.1. Fiber microstructure

Raman spectroscopy was used to investigate the fiber microstructure. A micro-Raman spectrometer with a 50 \times objective lens and an argon ion laser ($\lambda = 514.5$ nm) was used (spatial resolution = 2 μm and spectral resolution ≈ 2 cm^{-1}). Spectra were taken at every 5 μm until the whole diameter of the cross-section was covered. Analysis of the spectra as well as peak fitting was done with the GRAMS/32 program. This type of analysis has shown that there exists a radial change in the microstructure of the fibers [10,17,18]. The evolution of the Raman spectra with respect to fiber radius is shown in Fig. 2.

It can be seen that in the center ($r = 1$ μm) there is a very intense G peak ($\nu = 1581$ cm^{-1} , width = 29.9 cm^{-1}), a small D peak ($\nu = 1353$ cm^{-1} , width = 41.2 cm^{-1}) and

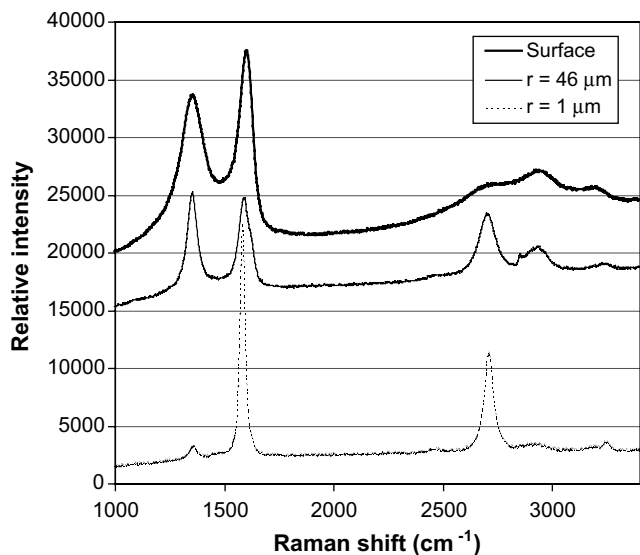


Fig. 2. Evolution of the Raman spectra with respect to fiber radius [17].

a $I(D)$ to $I(G)$ ratio of 0.05. This indicates the presence of a graphitic material close to single crystal graphite having a crystal grain size L_a of approximately 82,7 nm according to the Tuinstra–Koenig equation [19]. At the edge of the fiber ($r = 46 \mu\text{m}$), the intensity of the D peak ($\nu = 1352 \text{ cm}^{-1}$, width = 53.7 cm^{-1}) is lower than the intensity of the G peak ($\nu = 1588 \text{ cm}^{-1}$, width = 52.9 cm^{-1}) with a $I(D)$ to $I(G)$ ratio of 1.12 ($L_a = 3.9 \text{ nm}$). The increase of the G peak position, G and D peak width, $I(D)$ to $I(G)$ ratio and decrease of L_a , indicates the existence of a more disordered, turbostratic form of carbon with nano-dimensional ordering in the 'a' direction of stacked imperfect graphene sheets [20]. On the surface of the fiber, the G ($\nu = 1589 \text{ cm}^{-1}$, width = 69 cm^{-1}) peak and the D ($\nu = 1357 \text{ cm}^{-1}$, width = 184 cm^{-1}) peak are wider, have higher frequencies and the second order region is much less defined (wide bumps instead of peaks). There is also an $I(D)$ to $I(G)$ ratio of 1.44. According to Ferrari et al., this corresponds to the second stage of the amorphization trajectory where the degree of disorder increases significantly. In this stage, the G peak frequency and the $I(D)$ to $I(G)$ ratio decrease with an increase in the degree of amorphization after having reached a maximum. Hence, the changes in the D and G peak positions, widths and intensities outline the radial change in microstructure due to the laser's Gaussian power distribution. The distinct fiber regions can be seen from the cross-section in Fig. 3.

The microstructure changes depending on the incident laser power and the precursor pressure used during deposition. An increase in precursor pressure reduces graphitization [17]. An increase in laser power improves graphitization by increasing the temperature until a spe-

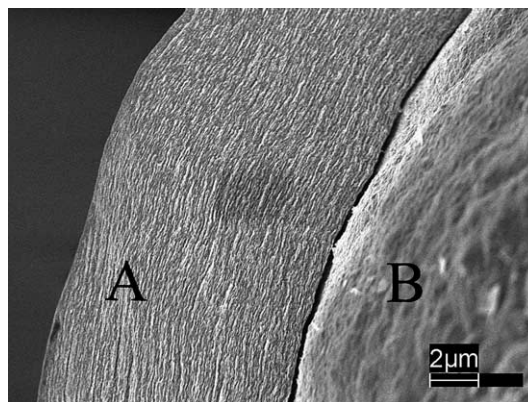


Fig. 3. Fiber cross-sectional regions: (A) edge region and (B) core region.

cific laser power value. Beyond this value, further increase in laser power will hinder graphitization due to an increase in linear growth rate brought about by higher temperatures [17,18]. A high growth rate hinders graphitization by reducing the residence time of the laser focus at a specific point of the fiber, therefore reducing the energy deposited to support crystal formation during growth. The threshold laser power value beyond which graphitization decreases with increasing laser power is referred to as the graphitization turning point.

3.2. Fiber fracture pattern

An investigation of the local mechanical properties, achieved by nanoindentation of the fiber cross-sections, has shown that the local elastic modulus and hardness decreases from edge to center [11]. The trend in local modulus is a direct consequence of the radial change in microstructure. The fibers are a combination of a softer core surrounded by a stiffer edge region. This composite nature is responsible for the specific fracture pattern observed.

Based on the fiber growth model by Arnold [21], as well as on the cross-sectional analysis, the fibers are modeled as a stacking of successive parabolic deposits. A parabolic deposit shape occurs since growth rate is highest at the center of the fiber (axial growth rate). The growth rate decreases away from the tip (lateral growth rate) as a result of the laser's Gaussian power distribution [22]. A periodic layered fiber structure was first observed by Nelson and Richardson [6], and later by Fauteux and Pegna [10]. Also, from a polished longitudinal section, a set of crack occurring periodically, following the surface of the fiber, were observed by Leyendecker et al. [22]. From the orientation of the deposit layers and the crack patterns, the fibers are not expected to have great strength [6].

Fig. 4 shows a model of the layered structure responsible for the fracture pattern. As stress is applied, the

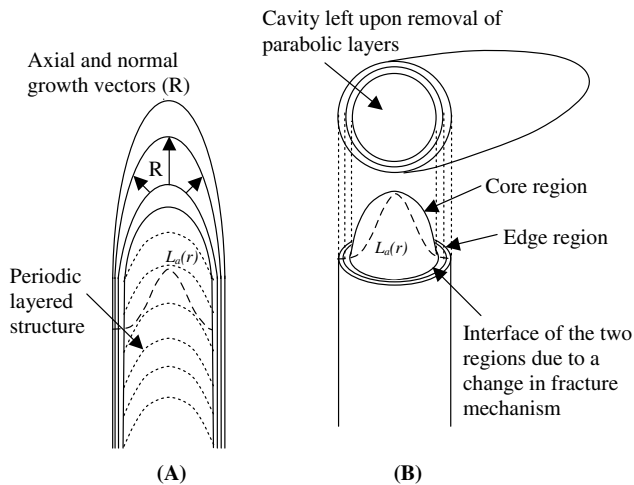


Fig. 4. (A) Layered fiber structure and (B) the fracture pattern leading to the creation of the two regions.

fibers deform and bend. The inside of the bend is under compression whereas the outside is under tension. Fracture occurs when axial strain equals the tensile breaking strain. The concentric layers in the edge region support the load and resist the strain until fracture. On the side being compressed, the induced stress causes disorder among the deposited layers in the edge region. This can be seen in Fig. 5C. The edge region has a brittle behavior due to transverse crack propagation and can collapse under the load as seen in Fig. 5D.

After fracture, residual parabolic layers in the core region were found. Separation occurs between the deposited layers. This can be seen in Fig. 5A. The

corresponding fiber end houses a cavity created upon removal of these parabolic layers as can be seen in Fig. 5B. The presence of the interface between edge and core regions marks a change in fracture mechanism due to a change in microstructure.

At higher laser powers and pressures a more even fracture was observed. This is explained by the fact that all the regions are less graphitized [17], making the fracture pattern in the core region similar to the one found in the edge region. Overall strength is improved by a reduced graphitization level which limits fracture propagation.

From these observed features, it can be said that LCVD carbon fibers are quite different from PAN or pitch-based carbon fibers. In contrast to commercial carbon fibers that exhibit graphitic layers oriented along the tensile axis, it was shown that the microstructure of LCVD fibers is heterogeneous. The fracture surface indicates that the material is ordered along parabolic fronts. However, it cannot be inferred that these parabolic patterns are the macroscopic manifestation of microstructural ordering of the graphitic layers without a thorough microstructural analysis such as transmission electron microscopy (TEM). There is no clear discussion of this observed macroscopic structure in the literature to date that would allow us to draw any clear conclusion regarding crystallite orientation. Thus, because of the radial change in microstructure, LCVD fibers cannot lend themselves to the analysis reserved for graphite carbon fibers. Nevertheless, it is clear from the fracture patterns observed that the fiber's layered structure influences the fracture behaviour.

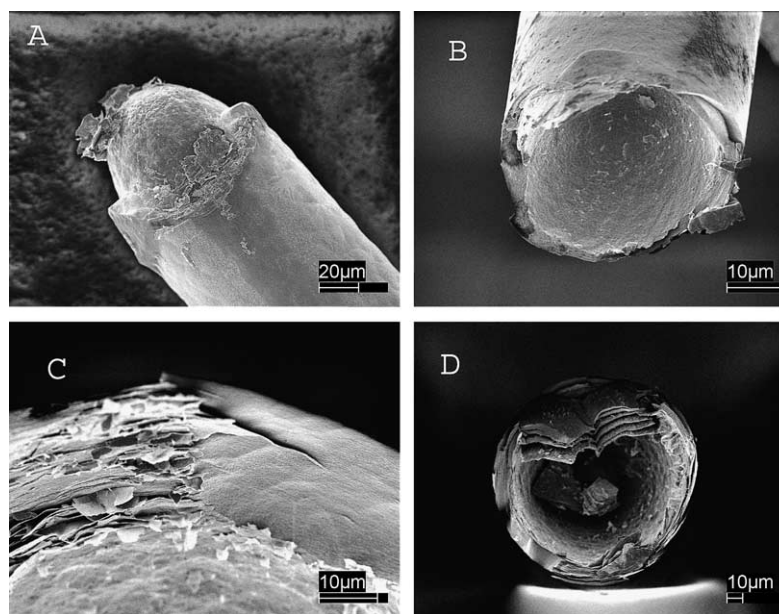


Fig. 5. Characteristic cleaving pattern observed: (A) core region's parabolic layers remaining after fracture; (B) cavity left in other fiber segment; (C) disturbed ordering of edge layers on compressed fracture face and (D) edge that has collapsed under the load.

3.3. Fiber region size dependence

At atmospheric and sub-atmospheric pressures, it has been observed that the different fiber regions vary in size. Fiber cross-sections were exposed by cleaving. The sizes of the edge and core regions were measured from SEM pictures. Different power settings were used at four constant pressures to deposit fibers. Figs. 6–9 shows the size d of the different regions as a function of laser power for specific pressures. More precisely, d represents the radius of the core and the thickness of the edge.

From these figures, it can be said that the core is the dominant fiber region. It represents 70–90% of the fiber radius. It increases in size with laser power for all pressures studied. Higher laser powers increase the temperature at the tip of the growing fiber, allowing the deposition of graphitic material ($L_a > 100 \text{ \AA}$) [17]. The edge also increases with laser power and does so significantly above 1.0 W. The size of the fiber regions, with respect to the whole fiber, was not significantly affected by pressure for the interval studied. Increasing the pressure decreases graphitization in every region of the fiber. Fiber region size differences can be seen in Fig. 10. In Fig. 10A, a very thin edge region with a pronounced parabolic structure is seen whereas Fig. 10B shows a thicker edge with flatter core.

3.4. Fiber morphology

At lower pressures and laser powers, the fibers were extremely smooth with very few surface defects. This can be seen in Fig. 11A. The formation of surface nodules occurred at higher laser powers and pressures as seen in 11B. This observation is significant since the surface morphology can influence the strength measurements. Based on fiber observations such as the fracture cross-section shown Fig. 10B, it can be seen that surface roughness does not extend deep into the edge region. Indeed, pronounced nodular features occur only on the surface of large diameter fibers. Approximately $10 \mu\text{m}$ in size, these surface features represent a small fraction

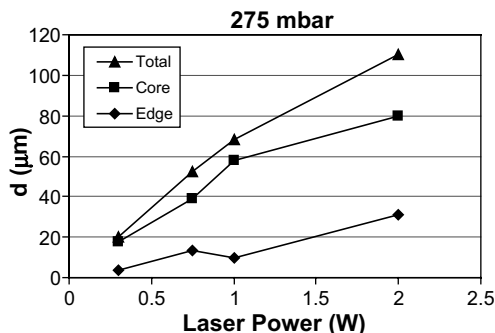


Fig. 6. Fiber region size vs. laser power at constant pressures.

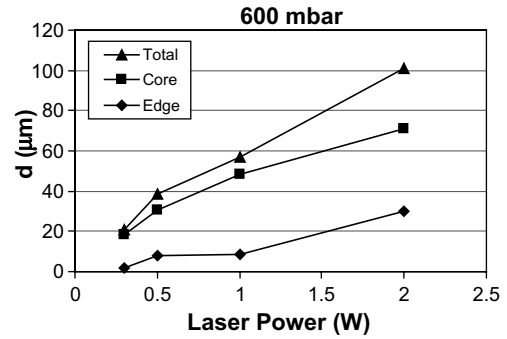


Fig. 7. Fiber region size vs. laser power at constant pressures.

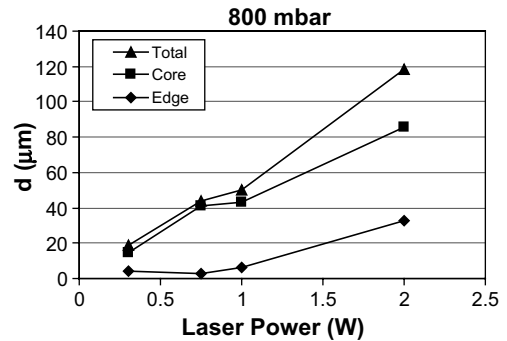


Fig. 8. Fiber region size vs. laser power at constant pressures.

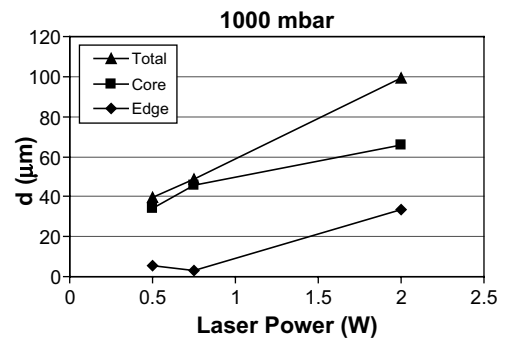


Fig. 9. Fiber region size vs. laser power at constant pressures.

of the fiber diameter (less than 5%). It is therefore doubtful that these features would influence the measurements.

3.5. Fiber quality

Examination of fiber fracture location has shown that fibers at higher pressures and higher laser powers have structural weaknesses. Indeed, these fibers fracture at a weakness point rather than at the center where the load is applied. This can be seen in Fig. 12.

Fiber quality is related to axial uniformity. Variation in diameter and noticeable structural defects occur during uncontrolled fiber growth. Precise manual focus

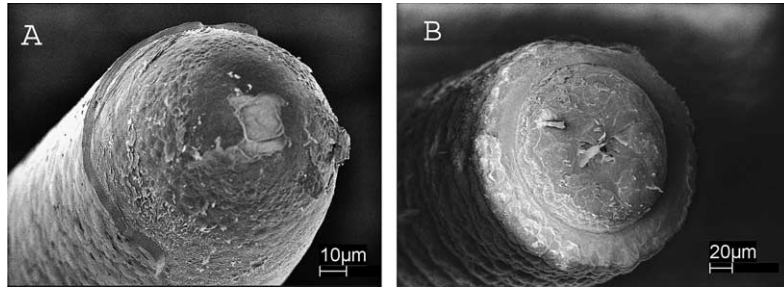


Fig. 10. Region size differences: (A) 0.75 W, 985 mbar and (B) 2.0 W, 600 mbar.

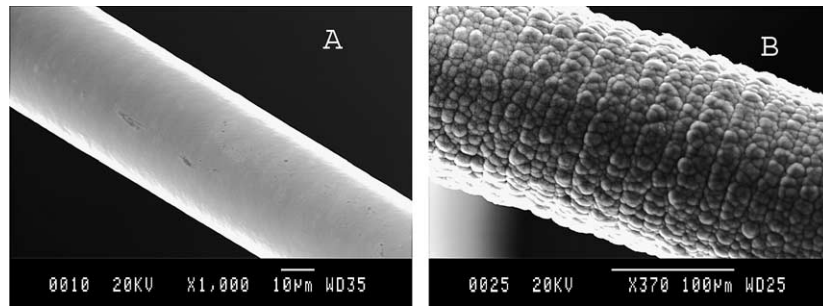


Fig. 11. Surface morphology comparison: (A) smooth fiber deposited at 0.3 W and 600 mbar and (B) very nodular surface at 2 W and 1000 mbar.

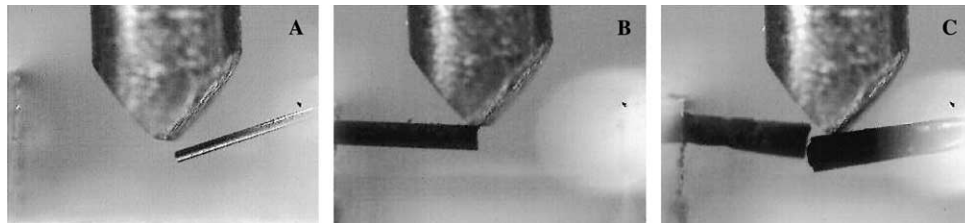


Fig. 12. Fiber fracturing: (A) 0.5 W, 800 mbar, $D = 77.9 \mu\text{m}$; (B) 1.0 W, 275 mbar, $D = 181.32 \mu\text{m}$ and (C) 2 W, 1000 mbar, $D = 243.1 \mu\text{m}$.

tracking becomes more difficult at higher pressures and laser powers due to an increase in the linear growth rate. A small misalignment in focus changes the power density in the reaction zone. This creates segments of the fiber that deposit under different conditions, hence have different microstructures. In this analysis, tracking difficulties occurred at powers beyond 1.0 W for most pressures except at 275 mbar. It is then clear that for superior fiber quality a high degree of process control must be achieved.

3.6. Micro-mechanical testing

Various loads were applied at the center of the fibers. Fiber selection was based on axial uniformity. Fig. 13 shows linear force-deflection curves for different fibers diameters. The deflection (δ) for a specific force (F) decreases with increasing fiber diameter (D). This shows

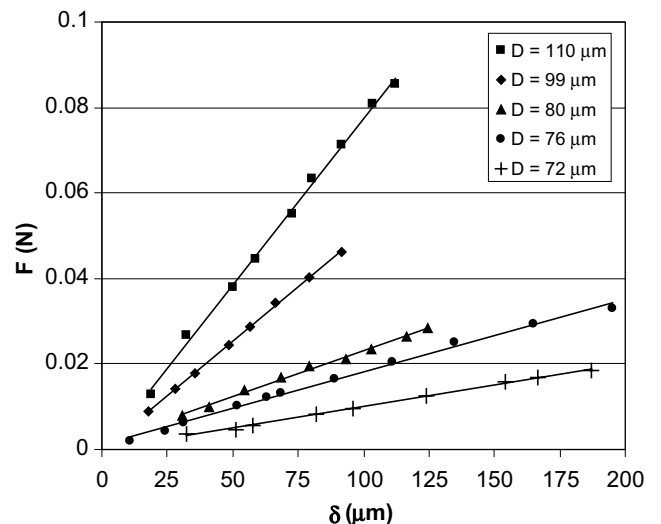


Fig. 13. Linear force-deflection curves.

how fiber stiffness increases with diameter. All fibers bent elastically until fracture even with an applied load close to the fracture threshold. No residual strain was observed upon retraction of the stylus.

3.7. Elasticity

The Young's modulus was calculated according to Eq. (1)

$$E = \frac{Fl^3}{12\pi\delta r^4} \quad (1)$$

where l is the distance between the outer supports, F is the load applied at the center, δ is the deflection and r is the fiber radius. Eq. (1) describes the bending behavior of a circular homogeneous beam with an applied load at the center. For this reason, the above equation is used as an approximation for the fiber's modulus since a varying microstructure is observed.

Fig. 14 shows two fibers at maximum deflection before fracture. Young's modulus values of 11–21 GPa were obtained depending on the deposition parameters. These values correspond to the maximum and minimum in local elastic modulus of LP-LCVD fibers found by nanoindentation [11]. The uncertainty in the modulus is 5–9% depending on the fiber.

3.7.1. Elastic modulus and graphitization

Bond structure and structural ordering will influence a material's stiffness. This is the case for single-crystal graphite which is much softer and has lower elastic modulus than the more disordered form of carbon. Since the bulk mechanical properties of the fibers will be influenced by their internal structure and its local mechanical properties, the Young's modulus' variation will be explained with respect to the level of graphitization reached in the fibers, which in this case is based on crystallite sizes measured by Raman spectroscopy. If the crystal grains are closer together and if they have a preferred orientation which is not parallel to the fracture propagation line, the strength will be locally reduced because of the anisotropic mechanical behaviour of

graphitic materials. Thus, the Young's modulus will decrease with an increase in the fiber's graphitization level.

As stated in Section 3.1, when laser power is increased, bigger crystallites will form, leading to larger crystalline domains that will locally reduce the strength of the fiber. This will decrease the value of Young's modulus measured until the graphitization turning point is reached. Beyond this point, the modulus is expected to increase since a higher linear growth rate will hinder graphitization.

The Young's modulus was plotted with respect to laser power for different pressures in Fig. 15. A general trend is observed: the moduli decrease with increasing laser power and reach a minimum before increasing again. This is in accordance with the expected variation induced by a change in microstructure.

The minimum and the maximum in Young's modulus change from one pressure to another. The minimum values of elastic modulus in Fig. 15 are *elastic modulus turning points*. They correspond to laser power values at which there is also a graphitization turning point. Indeed, the graphitization turning point at 1 bar was estimated to be near 0.5 W [17].

As the pressure is increased, the graphitization turning points occur at lower laser power values. For example, at 275 mbar the laser power can be increased well beyond 1.5 W before an increased growth rate begins to hinder graphitization. Since deposition at higher precursor pressures leads to higher growth rates and thus to a more disordered deposit, the maximum elastic modulus reached increases with pressure. This is easily observable at a laser power of 1 W. Lower values of Young's modulus occurred beyond 1 W for most pressures. These low values are attributed to poor fiber quality. For this reason, the fibers were removed from the analysis.

3.8. Fiber tensile strength

The three-point bending experiments showed our fibers to be brittle. In such a case, the ultimate fiber strength, σ , occurs at the end of the elastic domain

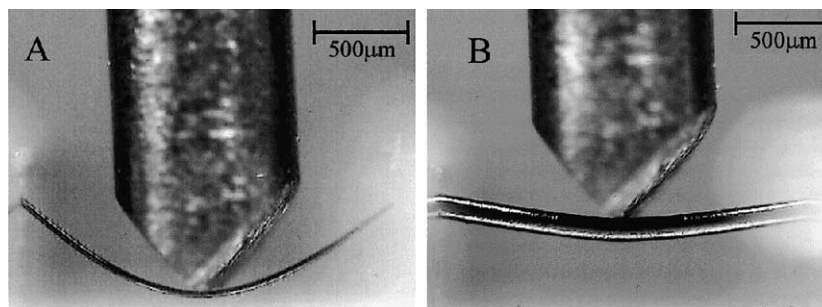


Fig. 14. Fibers bending under the stylus: (A) Fiber produced at 0.3 W, 1000 mbar, $D = 42.1 \mu\text{m}$ and (B) Fiber at 1.0 W, 275 mbar, $D = 125.4 \mu\text{m}$.

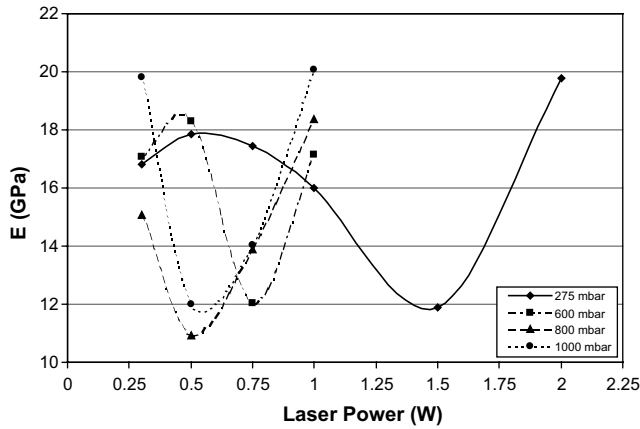


Fig. 15. Young's modulus vs. laser power at different pressures.

and its expression can be derived according to Eq. (2). Let F represent the bending moment and r be the fiber radius then

$$\sigma = \frac{4Fl}{\pi r^3}. \tag{2}$$

This expression assumes the material to be homogeneous and isotropic. It is then understood that Eq. (2) can only yield an average bulk material property in this case since the fiber microstructure changes within the fibers. However, one can test the validity of this model as the load should vary according to r^3 . The linear relationship exposed in Fig. 16 support this claim.

Under this assumption, the highest ultimate strength was found to be 0.82 GPa and the lowest was 0.57 GPa. The average value was 0.69 GPa. This result concurs with the tensile strength range reported by Wallenberger and Nordine [12,13]. Interestingly, when plotted with respect to radius, the strength value remains approximately constant. This is shown in Fig. 17. This is consistent with the fact that ultimate strength is a characteristic of the material and not of the geometry.

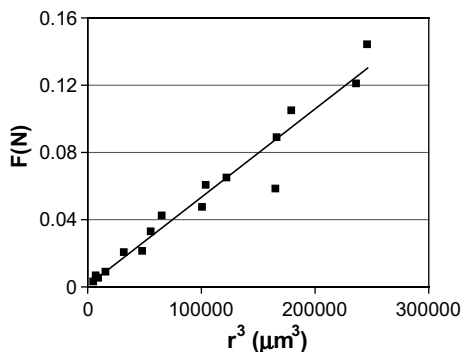


Fig. 16. Fracture force vs. r^3 .

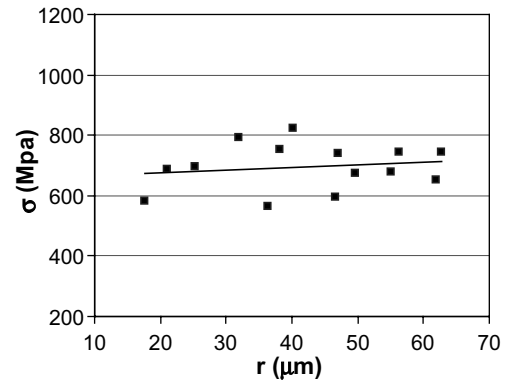


Fig. 17. Ultimate tensile strength vs. radius.

3.9. Bending strain

For three-point bending, the fibers deformation shape can be represented as a cubic curve. The minimum radius of curvature is obtained at the loading point and conforms to Eq. (3), in the same notation as above

$$\rho = \frac{E\pi r^4}{4Fl} \tag{3}$$

The maximum bending strains, $\epsilon = r/\rho$, is plotted against diameter and is shown in Fig. 18. The average maximum strain is 1%.

Again, it can be observed that the maximum bending strains remain more or less constant regardless of geometry. The range of process parameters is insufficient to show any marked variation in maximum strain.

4. Conclusion

LP-LCVD carbon fibers have poor mechanical properties when compared to PAN and pitch-based carbon fibers. Unlike PAN and pitch-based carbon fibers that exhibit preferred graphite layer orientation along the tensile axis, LP-LCVD fibers exhibit a broad range of microstructure and lack preferred orientation. The

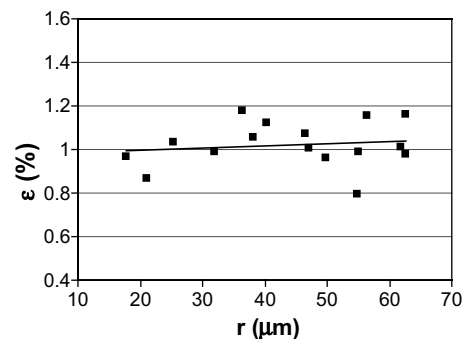


Fig. 18. Bending strain vs. diameter.

Young's modulus was found to vary according to the degree of graphitization reached in the fibers. An increase in Young's modulus is possible by decreasing graphitization. This is achieved at high reactor pressure and elevated laser powers which bring about high linear growth rates. Ultimate fiber tensile strength and bending strain do not vary significantly within the parameter range studied. The mechanical properties are also dependent on fiber quality. Quality is expressed in term of axial uniformity. It was found that process control is critical to the quality of the fibers.

Acknowledgments

The authors wish to acknowledge Anders Johansson for his help with the HR-SEM and Marcus Lehto for his help with the micro-manipulator's setup as well as for the creation of the LabView control program.

References

- [1] Lavin JG. Fracture of carbon fibers. In: Elices M, Llorca J, editors. *Fiber fracture*. Amsterdam: Elsevier; 2002. p. 158–79.
- [2] Dresselhaus MS, Dresselhaus G, Sugihara K, Spain IL, Goldberg HA. *Graphite fibers and filaments*. Berlin: Springer-Verlag; 1988. p. 122.
- [3] Wallenberger FT, Nordine PC, Boman M. Inorganic fibers and microstructures directly from the vapor phase. *Comput Sci Tech* 1994;51:193–212.
- [4] Pegna J, Messia D, Lee WH. Trussed structures: freeform fabrication without the layers. In: *Solid Freeform Fabrication Symposium Proceedings*; 1997. p. 49–58.
- [5] Leyendecker G, Bäuerle D, Geittner P, Lydtin H. Laser induced chemical vapor deposition of carbon. *Appl Phys Lett* 1981; 39(11):921–3.
- [6] Nelson LS, Richardson NL. Formation of thin rods of pyrolytic carbon by heating with a focused carbon dioxide laser. *Mater Res Bull* 1972;7:971–6.
- [7] Wallenberger FT. *Advanced inorganic fibers: processes, structures, properties, applications*. Boston: Kluwer Academic Publishers; 2000. p. 1–20.
- [8] Maxwell JL, Pegna J, Messia DV. Real-time volumetric growth rate measurements and feedback control of three-dimensional laser chemical vapor deposition. *Appl Phys A* 1998;67:323–9.
- [9] Jean D, Duty C, Johnson R, Bondi S, Lackey WJ. Carbon fiber growth kinetics and thermodynamics using temperature controlled LCVD. *Carbon* 2002;40:1435–45.
- [10] Fauteux C, Pegna J. Radial characterization of 3D-LCVD carbon fibers by Raman spectroscopy. *Appl Phys A* 2004;78(6):883–8. Published online September 16th, 2003. doi:10.1007/s00339-003-2084-x.
- [11] Longtin R, Fauteux C, Coronel E, Wiklund U, Pegna J, Boman M. *Appl Phys A* 2003;79:573–7. Published online January 21st 2004. doi:10.1007/s00339-003-2449-1.
- [12] Wallenberger FT. Inorganic fibres and microfabricated parts by laser assisted chemical vapour deposition. *Ceram Int* 1997;23: 119–26.
- [13] Wallenberger FT, Nordine PC. Strong, pure, and uniform carbon fibers obtained directly from the vapor phase. *Science* 1993;260: 66–8.
- [14] Greek S, Ericson F, Johansson S, Schweitz JÅ. In situ tensile strength measurement and Weibull analysis of thick film and thin film micromachined polysilicon structures. *Thin Solid Films* 1997;292:247–54.
- [15] Johansson S, Schweitz JÅ, Westberg H, Boman M. Microfabrication of three-dimensional boron structures by laser chemical processing. *J Appl Phys* 1992;72(12):5956–63.
- [16] Westberg H, Boman M, Johansson S, Schweitz JÅ. Freestanding silicon microstructures fabricated by laser chemical processing. *J Appl Phys* 1993;73(11):7864–71.
- [17] Fauteux C, Longtin R, Pegna J, Boman M. Microstructure and growth mechanism of laser grown carbon microrods as a function of experimental parameters. *J Appl Phys* 2004;95(5):2737–43. doi:10.1063/1.1641954.
- [18] Fauteux C, Longtin R, Pegna J, Boman M. Raman characterization of laser grown carbon microfibers as a function of experimental parameters. *Thin Solid Films* 2004;453–4:606–10. doi:10.1016/S0040-6090(03)01749-8.
- [19] Tuinstra F, Koenig JL. Raman spectrum of graphite. *J Chem Phys* 1970;53:1126–30.
- [20] Ferrari AC, Robertson J. Interpretation of Raman spectra of disordered and amorphous carbon. *J Phys Rev B* 2000;61: 14095–107.
- [21] Arnold N, Thor E, Kirichenko N, Bäuerle D. Pyrolytic LCVD of fibers: a theoretical description. *Appl Phys A* 1996;62:503–8.
- [22] Leyendecker G, Noll H, Bäuerle D, Geittner D, Lydtin H. Rapid determination of apparent activation energies in chemical vapor deposition. *J Electrochem Soc* 1983;130(1):157–60.